Biomaterials 203 (2019) 43–51

Contents lists available at ScienceDirect

Biomaterials

journal homepage: www.elsevier.com/locate/biomaterials

Intriguing "chameleon" fluorescent bioprobes for the visualization of lipid droplet-lysosome interplay

Rong Hu[a,1], Bin Chen[a,1], Zhiming Wang[a], Anjun Qin[a], Zujin Zhao[a,*], Xiaoding Lou[b,**], Ben Zhong Tang[a,c,***]

[a] State Key Laboratory of Luminescent Materials and Devices, Center for Aggregation-Induced Emission, South China University of Technology, Guangzhou, 510640, China
[b] Engineering Research Center of Nano-Geomaterials of Ministry of Education, Faculty of Materials Science and Chemistry, China University of Geosciences, 388 Lumo Road, Wuhan, 430074, China
[c] Department of Chemistry, Hong Kong Branch of Chinese National Engineering Research Center for Tissue Restoration and Reconstruction, The Hong Kong University of Science and Technology, Clear Water Bay, Kowloon, Hong Kong, China

ARTICLE INFO

Keywords:
Fluorescent bioprobe
Nanomaterials
Lipid droplet
Lysosome
Aggregation-induced emission

ABSTRACT

The interplay of lipid droplets (LDs) and lysosome plays an important role in cell metabolism, and the visualization of this process can provide useful information of organelle communication and function. However, fluorescent bioprobes based on organic fluorophores that can respond to LD-lysosome interplay are much rare. Herein, fluorescent bioprobes with high photostability, excellent biocompatibility and intracellular polarity sensitivity are achieved by encapsulating a new red fluorogenic molecule TPA-BTTDO within polymeric matrix (DSPE-PEG_{2000}). They can sequentially localize in lysosome and LDs with red and cyan emissions, respectively. By monitoring the emission color change, the interesting dynamic processes of the probes escaping from lysosome and then enriching in LDs, and finally returning to lysosome after LDs consumption are visualized. In addition, the tracing of dynamic movement and consumption of LDs is realized by the probes with a high signal-to-noise ratio. The unique labeling behaviors and distinguished dual emissions of the probes in LDs and lysosome make them promising agents for fluorescence visualization studies of LD-lysosome related bioprocess and metabolism diseases.

1. Introduction

Lipid droplet (LD), existing in the cytoplasm of most eukaryotic cells, is a well-connected organelle that regulates the storage and metabolism of neutral lipids. It has exhibited important multifunctions in energy generation and membrane formation in cells [1,2], and can prevent cells from lipotoxicity induced by the buildup of excess lipids, which is relevant to many diseases, such as obesity, type II diabetes, cardiovascular disease and virus infections [3–6]. Moreover, the level of LD has been regarded as a biomarker of cancer because of the great requirement of fatty acids and phospholipids during cancer growth [7,8]. Lysosome is another important cytoplasmic organelle that is present in all nucleated mammalian cells, and the functional deficiency of lysosome will result in many lysosomal storage disorders. It is acidic and contains various hydrolytic enzymes to break down kinds of biomolecules. Unwanted components inside and outside cells can be digested by lysosome, performing as a waste disposal and recycle system, to produce building block metabolites. Actually, LD is highly related to lysosome, and the components in LD can be degraded by lysosomal enzymes via autophagy, which is termed as lipophagy [9,10]. Recently, it is found that LD-lysosome interplay has strong affinities with chronic inflammation and metabolic diseases [11,12]. Therefore, the monitoring of LD and lysosome dynamic movements, metabolism and communication is of high significance to gain more valuable information for LD-lysosome interplay related diseases.

Respective researches on LD and lysosomes have been widely conducted over the past decades, such as movement tracking and formation mechanism observation [13–18]. Techniques based on molecular

* Corresponding author.
** Corresponding author.
*** Corresponding author. State Key Laboratory of Luminescent Materials and Devices, Center for Aggregation-Induced Emission, South China University of Technology, Guangzhou, 510640, China.
E-mail addresses: mszjzhao@scut.edu.cn (Z. Zhao), louxiaoding@cug.edu.cn (X. Lou), tangbenz@ust.hk (B.Z. Tang).
[1] These authors contribute equally.

https://doi.org/10.1016/j.biomaterials.2019.03.002
Received 7 November 2018; Received in revised form 25 February 2019; Accepted 1 March 2019
Available online 02 March 2019
0142-9612/

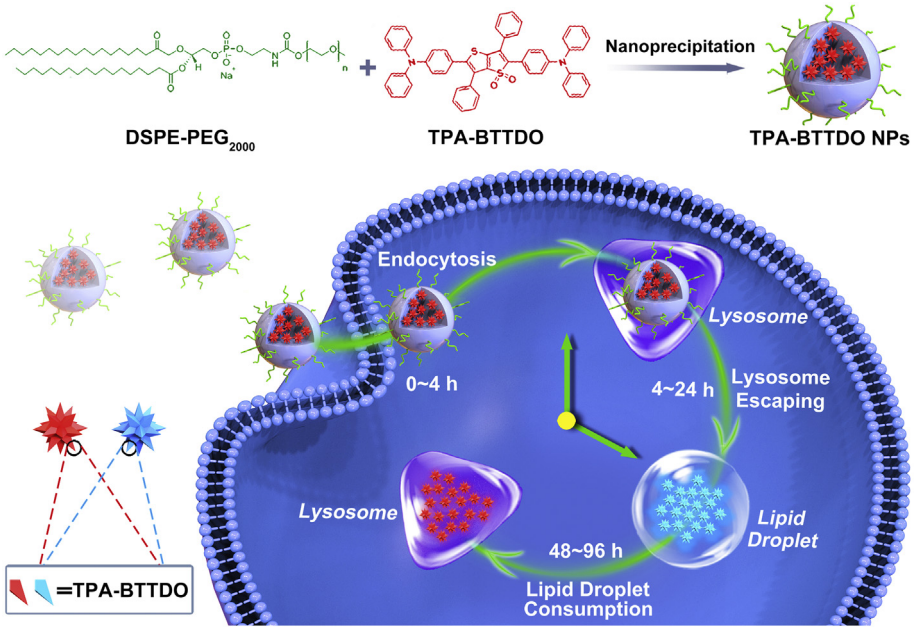

Fig. 1. The illustration of the internalization and consumption processes of TPA-BTTDO NPs in cells.

genetic analysis and biochemical reconstitution have been adopted to investigate the biological functions of LD and lysosome, however, their morphology and dynamic behavior cannot be visualized by these methods. Fluorescence imaging has demonstrated high sensitivity and non-invasive feature, and has become a powerful and widely used technique to study the dynamic process and functions of LD and lysosome [19–29]. Although fluorescent proteins had been reported to be used to study LD-lysosome interplay [29b], fluorescent probes based on organic fluorphores that can respond to LD-lysosome interplay for the application in fluorescence bioimaging are rarely reported. In this contribution, we develop a new red fluorogenic molecule (TPA-BTTDO) with aggregation-induced emission (AIE) property. Photostable and biocompatible fluorescent bioprobes are fabricated by encapsulating TPA-BTTDO within 1,2-distearoyl-*sn*-glycero-3-phosphoethanolamine-*N*-[methoxy(polyethylene glycol)-2000] (DSPE-PEG_{2000}) matrix by nanoprecipitation method. The generated bioprobes can sequentially localize in lysosome and LD, with red and cyan emissions, respectively. More importantly, by monitoring the emission color change, the escaping of the bioprobes from lysosome to LD, and finally get back to lysosome after LD metabolization are observed (Fig. 1), demonstrating the great potential for visualization of LD-lysosome interplay.

2. Results and discussion

The molecular structure of TPA-BTTDO is illustrated in Fig. 1, which is comprised of an electron-withdrawing thieno[3,2-b]thiophene S,S-dioxide (TTDO) core and electron-donating triphenylamine (TPA) groups [30a], indicating the molecule is prone to experience twisted intramolecular charge transfer (TICT) between TTPO and TPA, particularly in high polar environment. TPA-BTTDO can be facilely synthesized in a high yield. It is well soluble in common organic solvents such as THF, CH_2Cl_2, DMF and so on, but shows poor solubility in water. To improve the water dispersibility of TPA-BTTDO for bioimaging application, nanoparticles (NPs) of TPA-BTTDO are prepared by encapsulating it within DSPE-PEG_{2000} matrix via nanoprecipitation method. DSPE-PEG_{2000} is selected as the encapsulation matrix owing to its high water-solubility and excellent biocompatibility. As revealed by transmission electronic microscope (TEM) and dynamic light scattering (DLS), the resulting TPA-BTTDO NPs have a mean diameter of 52 nm and a hydrophobic diameter of 107 nm (Fig. S1). And a negative surface charge (−19 mV) of the NPs is also detected, resulting from the negatively charged DSPE-PEG_{2000}. No apparent change is found in size after the storing of TPA-BTTDO NPs for 360 h at PBS buffers (pH = 5 or 7) at 37 °C (Fig. S2), demonstrating that TPA-BTTDO NPs are highly stable. Besides, the concentration of DSPE-PEG_{2000} (4.8 μg/mL; 2.4×10^{-5} M) used in this work is much higher than its critical micelle concentration (0.2 μg/mL; 1×10^{-6} M) [30b], thus, TPA-BTTDO NPs also possess high stability at a lower concentration.

The fluorogenic molecule TPA-BTTDO shows absorption maximum at 463 nm with a molar absorptivity of 2.09×10^4 mol^{-1} L cm^{-1} and exhibits red emission peaking at 616 nm in THF solution (Fig. 2A). The emission wavelength of TPA-BTTDO is sensitive to the polarity of the environment. As the increase of solvent polarity, the emission peak is red-shifted progressively from 564 nm in hexane to 630 nm in DMF (Fig. 2B), which is attributed to the TICT effect. TPA-BTTDO can fluoresce efficiently in the aggregated state. The emission of TPA-BTTDO decreases along with a small red shift as the addition of a small amount of water into THF solution, which is attributed to the TICT in a more polar media. When the water fraction gets higher than 60%, most of the molecules start to form aggregate, in which the intermolecular motion is restricted and the nonradiative decay channel is blocked, resulting in enhanced emission, namely TPA-BTTDO has AIE property (Fig. 2C and D) [32–36]. TPA-BTTDO can also emit intensely at 614 nm in solid, with a high fluorescence quantum yield of 44.1%. Thanks to the AIE property, the TPA-BTTDO NPs show strong red emission at 611 nm, which are similar to those of TPA-BTTDO in aggregate or solid. The photostability and biocompatibility of TPA-BTTDO NPs are also evaluated. Upon exposure to 405 nm laser for 30 scans, the emission intensity of TPA-BTTDO NPs is only slightly decreased, while that of the control reagent BODIPY, a commercial LD probe, declines apparently, demonstrating that TPA-BTTDO NPs have much better photostability than BODIPY (Fig. 2E). The classical MTT assay is employed to investigate the biocompatibility, and the result shows that more than 95% cells are viable after incubation with TPA-BTTDO NPs for 24 h at a concentration range of 0.93–3.11 μg/mL, revealing the excellent biocompatibility (Fig. 2F). We have also evaluated the intracellular pH value of HeLa cells without and with the incubation of TPA-BTTDO NPs, and no obvious change can be observed, indicating the enrichment of TPA-BTTDO NPs in cells will hardly impact cells function (Fig. S3).

The confocal laser scan microscope (CLSM) is utilized to study the

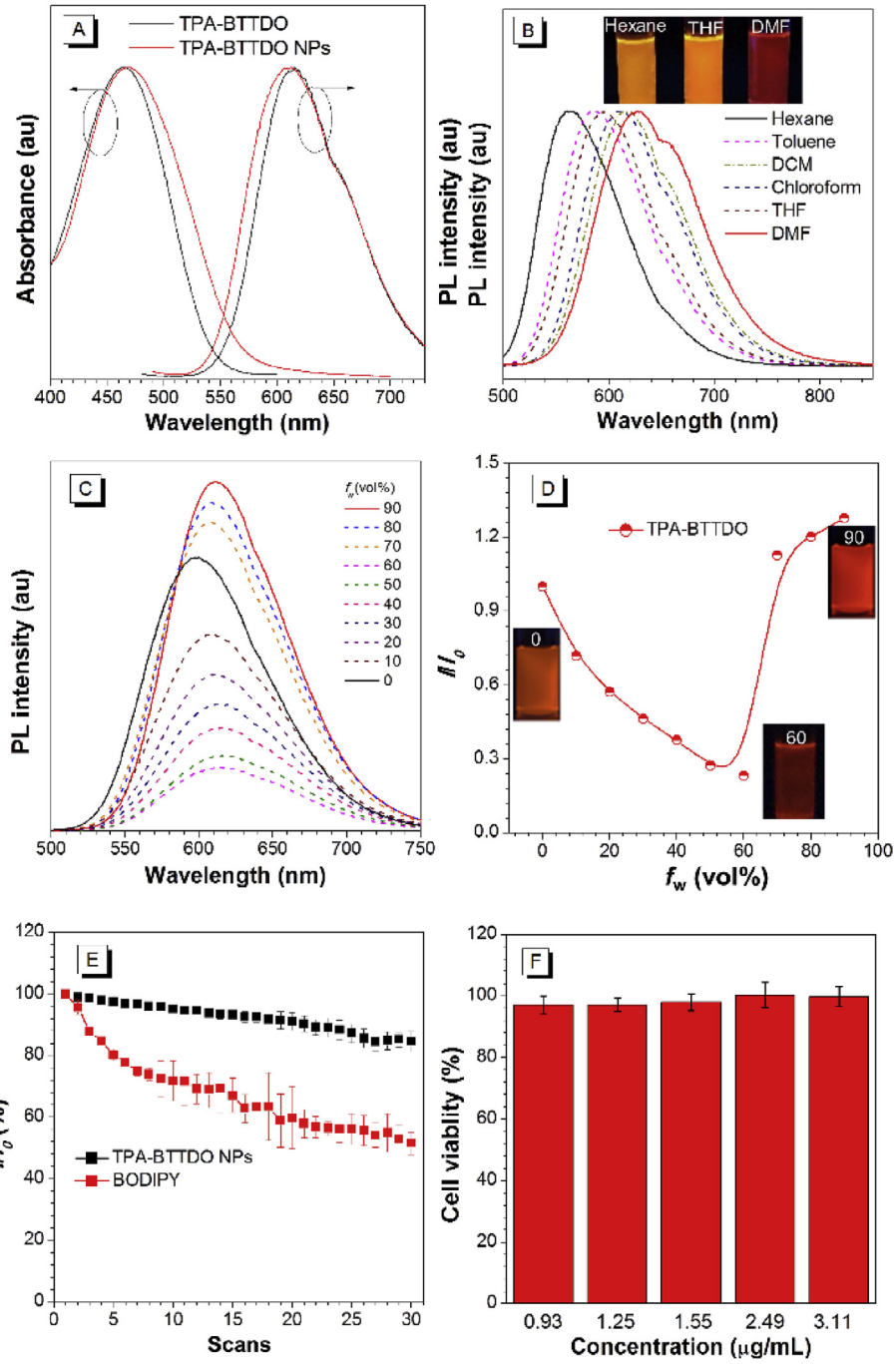

Fig. 2. (A) Absorption and photoluminescence (PL) spectra of TPA-BTTDO in THF solution and TPA-BTTDO NPs in water. (B) PL spectra of TPA-BTTDO in solvents with different polarity. (C) PL spectra of TPA-BTTDO in THF/water mixtures with different water fractions. (D) Plots of I/I_0 versus water fractions, where I_0 is the PL intensity in pure THF solution, inset: photos of TPA-BTTDO in THF/water (f_w = 0, 60 and 90%), taken under 365 nm excitation. (E) Photostability of TPA-BTTDO and BODIPY upon exposure to 405 nm laser with the intensity of 99%. (F) Viability of HeLa cells incubated with TPA-BTTDO NPs at different concentrations for 24 h.

staining behavior of TPA-BTTDO NPs towards cells, and HeLa cells are selected for the study. TPA-BTTDO NPs can successfully pass through the cell membrane after incubation at 37 °C (Fig. 3A and Fig. S4A). Upon co-staining with Lysotracker DND 99, it is found that only a small amount of TPA-BTTDO NPs localize in lysosome with an overlap coefficient of 0.55 ± 0.07 and a Pearson correlation coefficient of 0.52 ± 0.05. The majority of TPA-BTTDO NPs enrich in LDs as evidenced by the better colocalization with the commercial LD probe BODIPY (overlap coefficient = 0.63 ± 0.05; Pearson correlation coefficient = 0.57 ± 0.04) (Fig. 3C and Fig. S4B). In order to further confirm the selectivity of TPA-BTTDO NPs between LD and lysosome, HeLa cells are treated with oleinic acid to induce the formation of LDs intracellularly, and then incubated with TPA-BTTDO NPs. As shown in Fig. 3E, an even better colocalization (overlap coefficient = 0.86 ± 0.02; Pearson correlation coefficient = 0.85 ± 0.02) of TPA-BTTDO NPs with BODIPY is observed. The line series analysis for each group further verifies this specific labelling behavior (Fig. 3B, D and F). These imaging results indicate that although TPA-BTTDO NPs can enrich in both lysosome and LD, they prefer to localize in LDs. We have also investigated the enrichment of TPA-BTTDO NPs in normal cells of NIH 3T3 and kidney cancer cells of ktr-3, and similar phenomena of localization in lysosome and LDs are observed as well (Fig. S5).

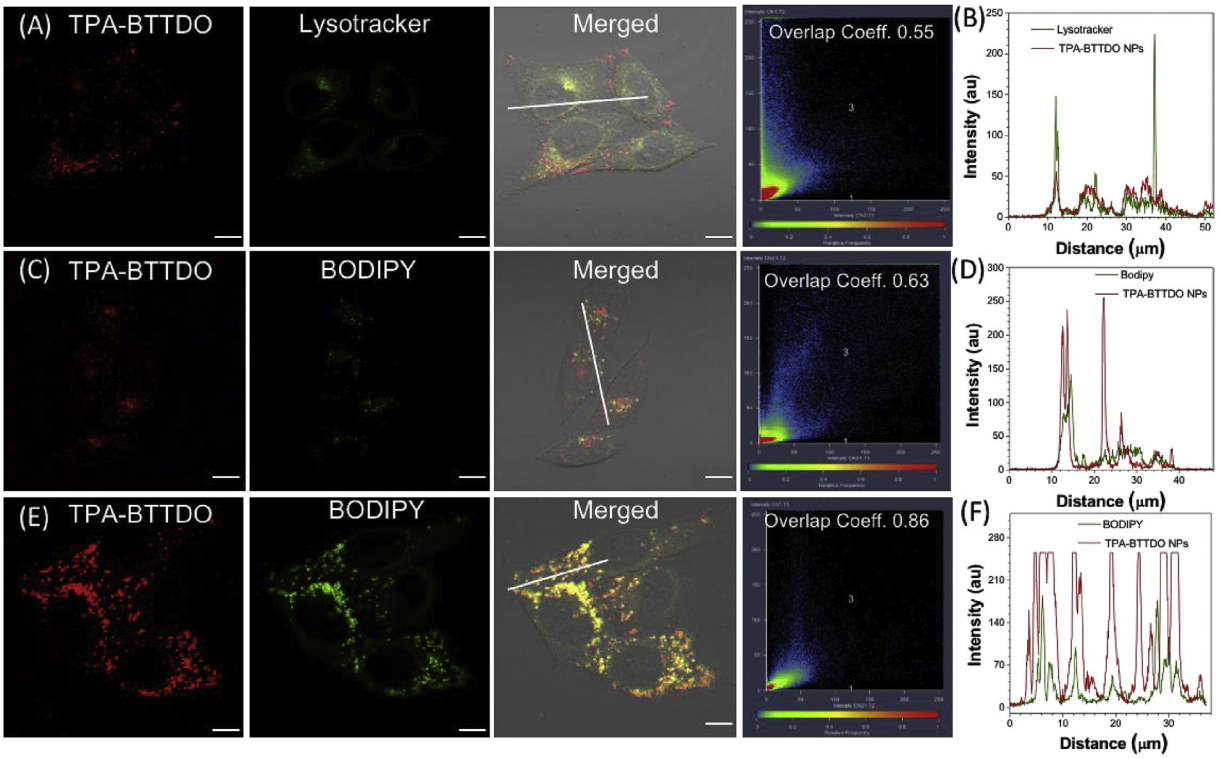

Fig. 3. CLSM images of HeLa cells incubated with TPA-BTTDO NPs followed by co-staining with (A) Lysotracker and (C) BODIPY. (E) CLSM images of HeLa cells incubated with TPA-BTTDO NPs after treated by oleic acid, followed by colocalization with BODIPY. Line series analysis for TPA-BTTDO NPs with (B) Lysotracker, (D) BODIPY and (F) BODIPY in cells treated by oleinic acid. [TPA-BTTDO NPs] = 2.4 μg/mL, [Lysotracker] = 100 nM, [BODIPY] = 10 μg/mL. TPA-BTTDP is highlighted in red; Lysotracker and BODIPY are highlighted in green. Scale bar = 10 μm.

To investigate the enrichment process of TPA-BTTDO NPs in LDs, HeLa cells incubated with TPA-BTTDO NPs for different times are studied under CLSM. As shown in Fig. 4, after 2 h incubation, intense red emission of TPA-BTTDO NPs can be detected, which is well overlapped with the emission of Lysotracker and shows relatively low colocalization with BODIPY, indicating that TPA-BTTDO NPs can pass through cell membrane within 2 h and localize in lysosome at first. Interestingly, after 4 h incubation, the colocalization efficiency of TPA-BTTDO with Lysotracker decreases, as the overlap coefficient and Pearson correlation coefficient reduce gradually (Fig. S6), and an obvious enhancement of overlap with BODIPY is observed (overlap coefficient = 0.70 ± 0.02; Pearson correlation coefficient = 0.68 ± 0.03) at the same time, demonstrating the localization of TPA-BTTDO in LDs increases. By further elongating the incubation time, more and more TPA-BTTDO escapes from lysosome and then enriches in LDs, rendering greatly intensified emission, while the emission in lysosome becomes weak. The overlap coefficient of TPA-BTTDO with BODIPY increases from 0.45 to 0.87, while that of TPA-BTTDO with Lysotracker decreases from 0.63 to 0.56 at the same time. By combining the selective staining behavior, we believe that TPA-BTTDO can escape from lysosome and then enter LDs.

As discussed above, TPA-BTTDO NPs initially localize in lysosome, thus, we speculate that NPs penetrate the cell membrane via endocytosis process. To confirm the internalization mechanism of TPA-BTTDO NPs in HeLa cells, the endocytosis inhibition assay is employed. In experimental groups, HeLa cells are treated under different endocytosis inhibition conditions, including low-temperature incubation and other inhibitor treatments of chlorpromazine, cytochalasin. D, nystatin, dynasore and sucrose, before the incubation with TPA-BTTDO NPs. Herein, chlorpromazine can inhibit the clathrin-mediated endocytosis, and nystatin has great depression effect on endocytosis based on caveolae. Besides, sucrose and cytochalasin. D can block receptor and actin mediated endocytosis, respectively. At 4 °C, the emission signal of TPA-BTTDO NPs is barely recorded (Fig. S7), as the endocytosis process is inhibited by energy blocking under low temperature. Meanwhile, among the different inhibitor treatments, only dynasore shows strong inhibition efficiency, indicating that dynamin-mediated endocytosis is the primary driving force for internalization process of TPA-BTTDO NPs. Therefore, TPA-BTTDO NPs will localize in lysosome before accumulation in LDs. According to the time-dependent internalization process in LDs, it is reasonable that TPA-BTTDO NPs will pass through the cell membrane via endocytosis and localize in lysosome at first, and then they will escape from lysosome and subsequently be internalized in LDs. Since there are complicated enzymes in lysosome, the DSPE-PEG_{2000} matrix may be decomposed. The resulting highly hydrophobic bare TPA-BTTDO prefer to accumulate in LDs because of the similar hydrophobic nature, which probably accounts for the interesting staining behaviors [27b].

More interestingly, by using Lambda-scanning under CLSM, dual emission property of TPA-BTTDO NPs is observed. By respective colocalization observation, high overlap coefficient (0.86 ± 0.03) and Pearson correlation coefficient (0.84 ± 0.02) are detected when TPA-BTTDO with cyan fluorescence colocalized with BODIPY, demonstrating that cyan fluorescent TPA-BTTDO enriches in lipid droplet. Meanwhile, upon colocalization with Lysotracker, perfect overlap coefficient (0.87 ± 0.05) and Pearson correlation coefficient (0.83 ± 0.03) are also observed for red fluorescent TPA-BTTDO. Thus, we can verify that TPA-BTTDO with cyan emission localizes in lipid droplet and TPA-BTTDO with red fluorescence enriches in lysosome (Fig. 5A and C). By studying the spectrum, TPA-BTTDO NPs show cyan emission (498 nm) in LDs, while red emission (614 nm) in lysosome (Fig. 5B and D). This should be caused by the different polarity of lysosome (high polarity) and LD (low polarity). To further confirm this, the emissions of TPA-BTTDO in cholesteryl oleate and glycerol trilaurate, the main components of LDs, are measured. As expected, TPA-BTTDO exhibits apparently blue-shifted emission at 588 nm in these environments, which is close to that in non-polar hexane (562 nm) (Fig.

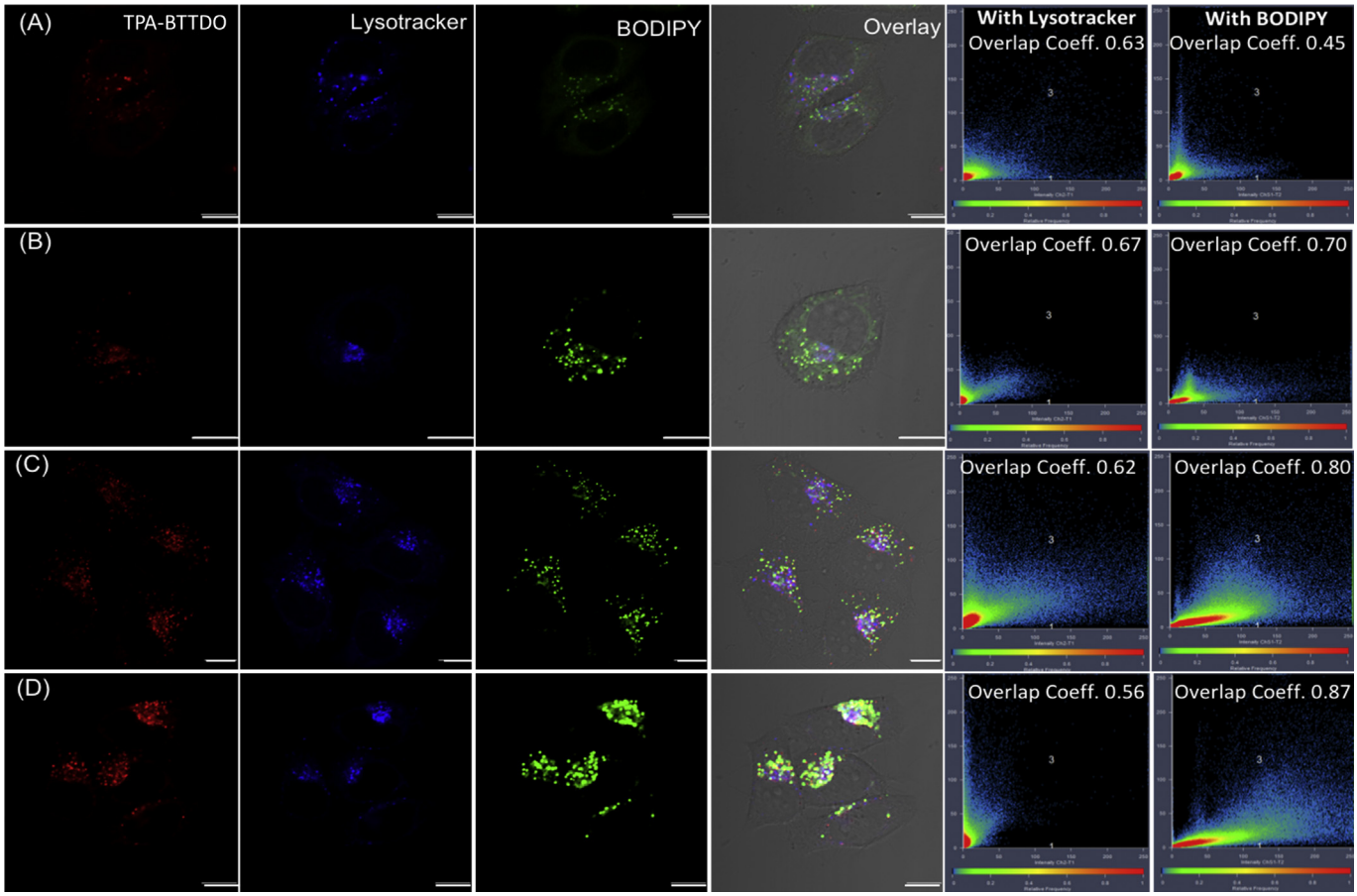

Fig. 4. CLSM images of HeLa cells incubated with TPA-BTTDO NPs for 2 (A), 4 (B), 12(C) and 24 h (D), respectively, followed by co-staining with BODIPY and Lysotracker. The overlap coefficient values of TPA-BTTDO NPs with Lysotracker and BODIPY were calculated. [TPA-BTTDO NPs] = 2.4 μg/mL, [BODIPY] = 10 μg/mL, [Lysotracker] = 100 nM. TPA-BTTDO is highlighted by red, BODIPY is highlighted in green, and Lysotracker is highlighted by blue. Scale bar = 10 μm.

S8). These findings imply that the polarity variation of the environments could be a major reason for the distinct emission color change of TPA-BTTDO. In addition, the components in LD should be much more complicated, which are also responsible for the bluer emission of TPA-BTTDO in LD (498 nm). Similar phenomena had been observed for many other fluorescent probes with donor-accepter structures [31a,36]. Nevertheless, this interesting "chameleon" behavior is quite promising for specific monitoring dynamic process of LDs.

Since LDs are highly dynamic organelles, and their movements along the skeleton of cells are of close relationship with membrane

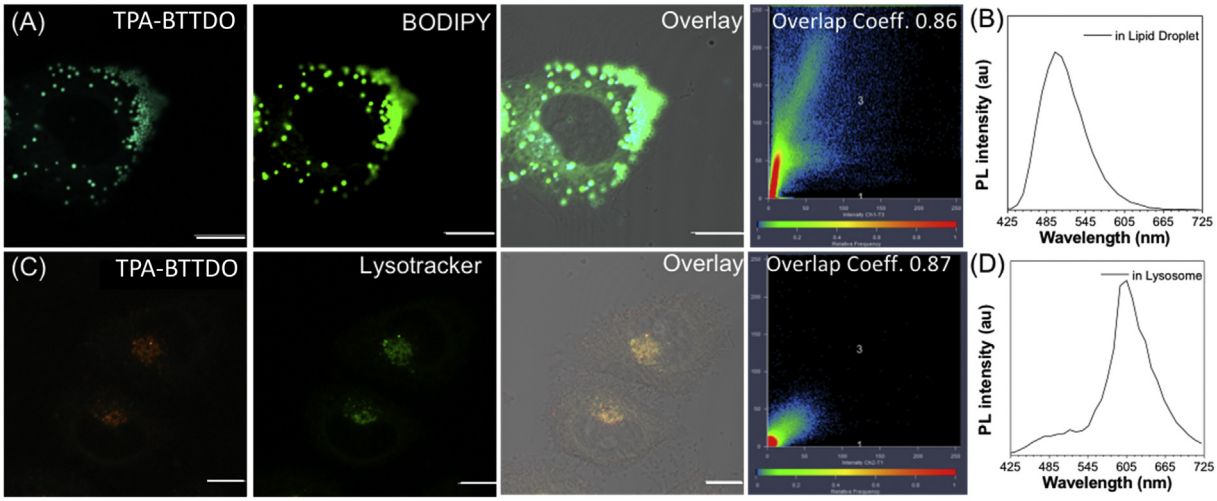

Fig. 5. Colocalization of cyan and red fluorescent TPA-BTTDO with BODIPY and Lysotracker, respectively. (A) Lambda-scanning images of HeLa cells labeled by cyan fluorescent TPA-BTTDO, followed with the co-stain with BODIPY. (B) The PL spectrum of TPA-BTTDO in lipid droplets. (C) Lambda-scanning images of HeLa cells labeled by red fluorescent TPA-BTTDO, followed with the co-stain with Lysotracker. (D) The PL spectrum of TPA-BTTDO in lysosome. [TPA-BTTDO NPs] = 2.4 μg/mL λ_{ex} = 405 nm; λ_{em} = 450–725 nm [BPDIPY] = 10 μg/mL, λ_{ex} = 488 nm; λ_{em} = 510–540 nm [Lysotracker] = 100 nM, λ_{ex} = 543 nm; λ_{em} = 570–700 nm. Scale bar = 10 μm.

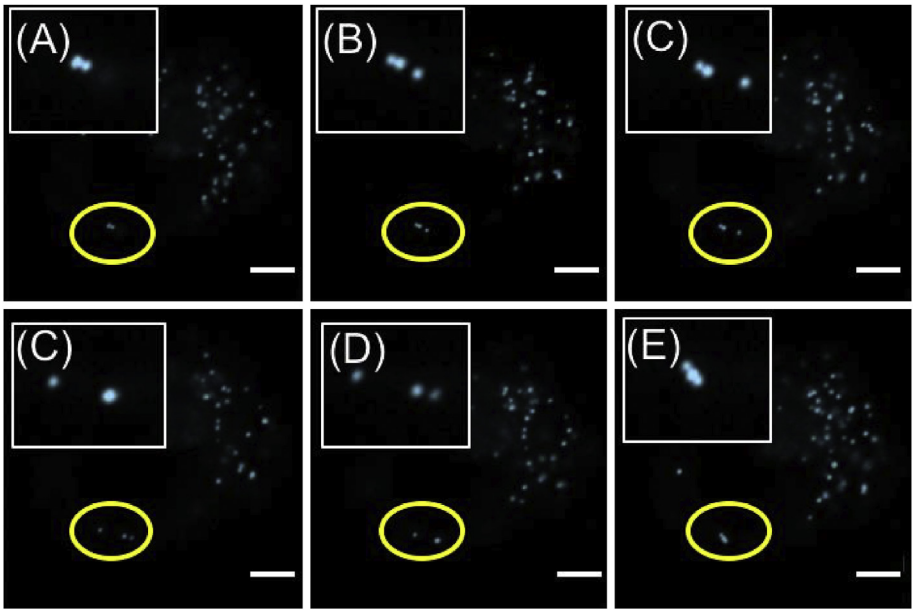

Fig. 6. CLSM images of HeLa cells stained with TPA-BTTDO NPs to illustrate the fluorescence images at different times of 0 min (A), 2 min (B), 4 min (C), 7 min (D), 8 min (E) and 10.5 min (F). [TPA-BTTDO NPs] = 2.4 μg/mL. The images in white frame in the upper left are the amplified images denoted by yellow circle. Scale bar = 5 μm.

synthesis and protein degradation, the dynamic movements of LDs are monitored based on the unique staining behavior as well as good photostability of TPA-BTTDO NPs. As shown in Fig. 6, the spatial distribution of LDs in HeLa cells can be observed easily at different stages, and their dynamic movements are traced with a high signal-to-noise ratio. As denoted by the yellow circles with the amplified images in white frames, the fusion and division processes of LDs are clearly visualized by monitoring the emission signal of TPA-BTTDO NPs, which can barely be observed under bright field.

In addition, the intracellular consumption of LDs can also be well distinguished with TPA-BTTDO NPs. As displayed in Fig. 7A, TPA-BTTDO NPs are successfully accumulated in LDs and exhibit bright cyan emission at the first day. Then, weak red emission can be detected on the second day. This phenomenon becomes more evident along with the extension of incubation time. At the fourth day, only red emission can be observed and the cyan emission disappears, demonstrating no TPA-BTTDO localize in LDs at this time. It is well known that LD has a close association with mitochondria because LD is an alternative resource for intracellular energy. And the consumption of LDs naturally results in the failure of localization of TPA-BTTDO in LDs. Meanwhile, lysosome can act as an important waste disposal system inside cells for biomolecules and unwanted materials digestion. Thus, the colocalization of TPA-BTTDO NPs with Lysotracker and Mitotracker are conducted, respectively. Delightfully, a perfect colocalization of TPA-BTTDO (red emission) with Lysotracker (green emission) is observed (overlap coefficient = 0.85 ± 0.02; Pearson correlation coefficient = 0.84 ± 0.02) (Fig. 7B, C and Fig. S9). These findings indicate that LDs are consumed and TPA-BTTDO are transferred into lysosome after LD consumption, owing to the stomach activity of lysosome.

In comparison with the fluorescent proteins expressed in lysosome and LD, these new fluorescent probes in this work possess several advantages for the study of LD-lysosome interplay. First, the labeling procedures for TPA-BTTDO NPs are quite simple, while the complicated transfection process is needed for fluorescent proteins. Second, the labeling efficiency of TPA-BTTDO NPs can reach 100%, but fluorescent protein generally only shows 50–80% labeling efficiency. Third, TPA-BTTDO NPs have perfect biocompatibility, but the transfection process often results in high cytotoxicity due to the use of Lipo 2000. Fourth, one fluorescent probe TPA-BTTDO shows dual emission when located in lysosome and LD, respectively, which can be more easily used to study the dynamic process by monitoring the fluorescence change. Clearly, TPA-BTTDO NPs hold a great potential in monitoring dynamic process for biofunctional observation of LD-lysosome interplay.

3. Conclusions

In summary, we have developed unique fluorescent probes (TPA-BTTDO NPs) for LD dynamic movement tracing and consumption. The TPA-BTTDO NPs fabricated by encapsulating the fluorogenic molecule TPA-BTTDO that possesses AIE and TICT features within DSPE-PEG_{2000} matrix show bright red emission, high photostability, excellent biocompatibility and intracellular-polarity sensitivity. They can be internalized by cells via dynamin-mediated endocytosis, and localize in lysosome, followed by escaping from lysosome and then accumulating in LDs. When LDs are consumed, they can finally return to lysosome. By utilizing Lambda-scanning mode, red and cyan emissions are detected in lysosome and LDs, respectively, which is attributed to the environmental polarity variation. The tracing of dynamic movement and consumption of LDs are visualized by TPA-BTTDO NPs with a high signal-to-noise ratio. These intriguing “chameleon” bioprobes could be an ideal candidate in fluorescence visualization of LDs for the investigation of biological functions, and holds a great potential in prevention of LDs-lysosome related metabolism diseases.

4. Experimental

4.1. Materials and measurements

All chemicals and reagents were purchased from commercial sources and used as received without further purification. ^{1}H and ^{13}C NMR spectra were measured on a Bruker AV 500 spectrometer in appropriated deuterated solution at room temperature. High resolution mass spectra (HRMS) were recorded on a GCT premier CAB048 mass spectrometer operating in MALDI-TOF mode. UV–vis absorption spectra were measured on a Shimadzu UV-2600 spectrophotometer. Photoluminescence spectra were recorded on a Horiba Fluoromax-4 spectrofluorometer. Fluorescence quantum yields were measured using a Hamamatsu absolute PL quantum yield spectrometer C11347 Quantaurus_QY. Confocal laser scanning microscope (CLSM) characterization was conducted with a confocal laser scanning biological microscope (LSM 710, Zeiss, Germany). The absorbance for MTT analysis was recorded on a microplate reader (Thermo Fisher, USA) at a wavelength of 570 nm. Size and zeta potential measurements were conducted on Dynamic Light Scattering (ZSE, Malvern, UK).

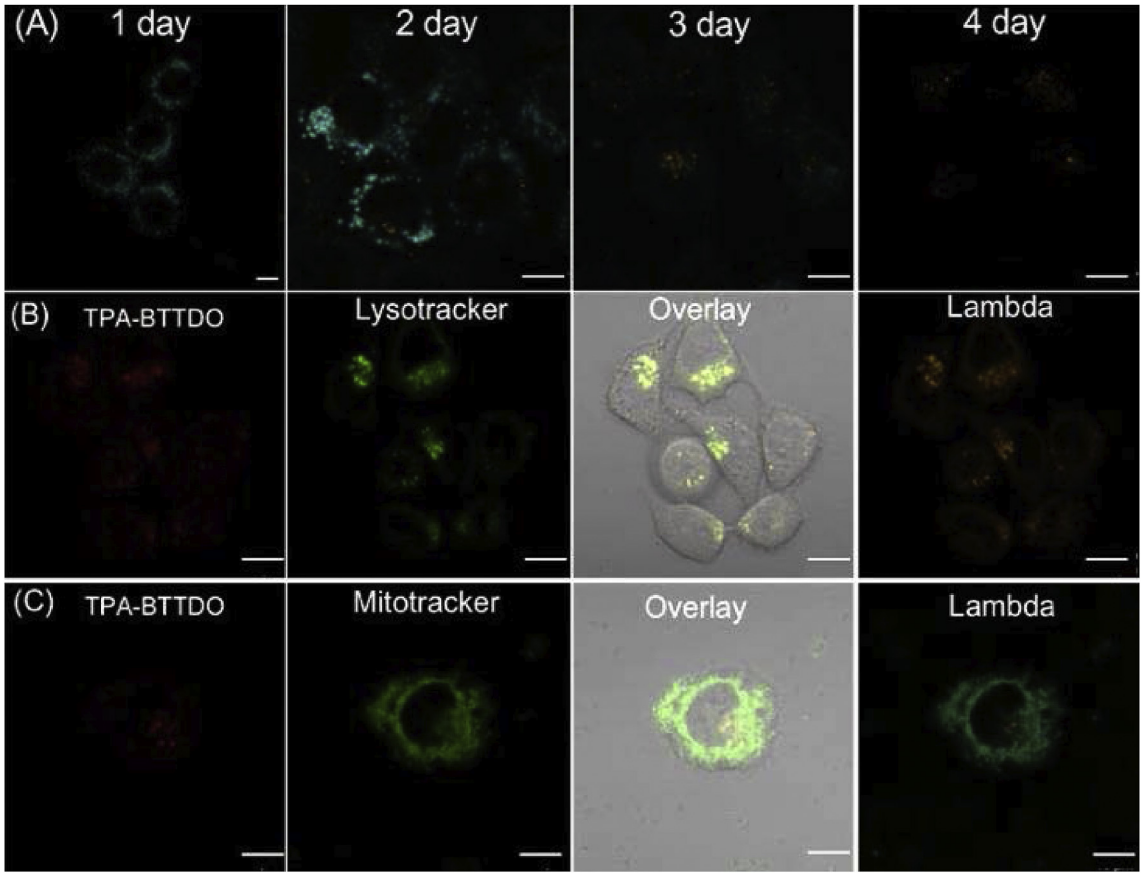

Fig. 7. The consumption process of TPA-BTTDO NPs in HeLa cells. (A) Lambda-scanning images of HeLa cells after incubated with TPA-BTTDO NPs during 4 days. CLSM images of HeLa cells after incubating with TPA-BTTDO NPs on the fourth day, followed by co-staining with (B) Lysotracker and (C) Mitotracker. [TPA-BTTDO NPs] = 2.4 μg/mL; [Lysotracker] = 100 nM; [Mitotracker] = 1 μM. TPA-BTTDO is highlighted in red; (B) Mitotracker and (C) Lysotracker are highlighted in green. Scale bar = 10 μm. (For interpretation of the references to color in this figure legend, the reader is referred to the Web version of this article.)

Nanoparticles were prepared on cell crusher (Qsonica Sonicators, USA). Automated cell counter (Countess II, Invitrogen) was employed for cell counting. Transmission electron microscope was carried on JEM-1400 Plus (JEOL, Japan). HeLa cells, NIH 3T3 cells and ktr-3 cells were obtained from cell culture center of Institute of Basic Medical Sciences, Chinese Academy of Medical Science (Beijing, China). PBS buffer, DMEM (Dulbecco's modified Eagle medium) and fetal bovine serum (FBS) were purchased from Thermo Fisher Scientific (Shanghai, China). Lysotracker DND 99, Mitotracker, pHrodo Red AM and BODIPY were purchased from Thermo Fisher Scientific (Shanghai, China). Water was purified with a Millipore filtration system. MTT was purchased from Tiangen Biotech (Beijing, China).

4.2. Synthesis

2,5-Bis(4-(diphenylamino)phenyl)-3,6-diphenylthieno[3,2-b]thiophene 1,1-dioxide (TPA-BTTDO): Compounds **2** (0.54 g, 1.11 mmol) and 3 (0.96 g, 3.39 mmol), $Pd(PPh_3)_4$ (0.13 g, 0.12 mmol) and K_2CO_3 (0.63 g, 4.53 mmol) were added in 100 mL two-necked bottle under a flow of nitrogen (Scheme 1). After then, a mixed solvent system of toluene, C_2H_5OH and H_2O (v/v/v = 8:1:1) was injected into the bottle, and the reaction mixture was refluxed for 12 h under nitrogen atmosphere. After cooling to room temperature, the mixture was poured into water and extracted twice with dichloromethane. The combined organic layers were washed successively with brine and water, and then dried over anhydrous magnesium sulfate. After filtration, the solvent was evaporated under reduced pressure and the residue was purified by silica-gel column chromatography using dichloromethane/hexane as eluent. Red solid of TPA-BTTDO was obtained in 89% yield. ^{1}H NMR (500 MHz, $CDCl_3$), δ (TMS, ppm): 7.60–7.57 (m, 2H), 7.54–7.51 (m, 2H), 7.45–7.41 (m, 3H), 7.40–7.31 (m, 5H), 7.30–7.23 (m, 9H), 7.15–7.01 (m, 13H), 6.92–6.87 (m, 4H). ^{13}C NMR (125 MHz, $CDCl_3$), δ (TMS, ppm): 148.92, 148.17, 147.04, 146.75, 144.81, 141.66, 137.96, 137.55, 132.91, 132.30, 132.17, 129.88, 129.72, 129.67, 129.44, 129.40, 129.29, 128.78, 128.47, 128.37, 125.90, 125.59, 125.13, 124.05, 123.69, 121.97, 121.10, 119.91. HRMS ($C_{54}H_{38}N_2O_2S_2$): *m/z* 810.2406 (M^+, calcd 810.2375).

4.3. The preparation of nanoparticles

TPA-BTTDO (3 mg) was dissolved in 1 mL of THF (Solution A), and DSPE-PEG_{2000} (3 mg) was dissolved in 1 mL of THF (Solution B). Solution A (300 μL) and Solution B (600 μL) were mixed uniformly, followed by the addition of 9 mL water under ultrasound. THF in mixture was removed by N_2 and dialysed with a membrane with molecular weight cutoff of 3500 g/mL. At last, the solution was filtered by a filter with the size of 0.22 μm.

4.4. Cell viability assay

HeLa cells were seeded in 96-well plate with 8×10^3 cells per well, and incubated with TPA-BTTDO NPs in DMEM (10% FBS) with the final concentration ranging from 0 to 3.1 μg/mL (100 μL/well), respectively. 24 h later, 100 μL of MTT (10 μM) in DMEM (10% FBS) was added, and 4 h incubation was needed. After removing the culture medium, 100 μL of DMSO was added to every well. The absorption was recorded by a microplate reader at 570 nm after shaking for 2 min. The cell viability ratio (VR) was evaluated according to the following equation:

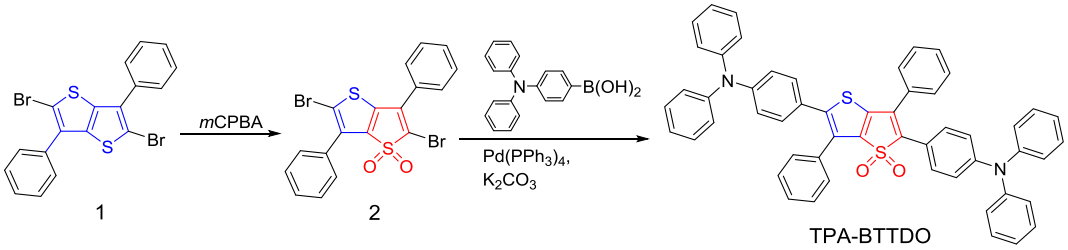

Scheme 1. Synthetic routes of TPA-BTTDO.

$$VR = \frac{A}{A_0} \times 100\%$$

Where A_0 is the absorbance of cells without any drugs, and A is the absorbance of cells incubated with TPA-BTTDO NPs.

4.5. The CLSM characterization of cells treated by TPA-BTTDO NPs

Normal incubation: HeLa cells were incubated with TPA-BTTDO NPs (2.4 μg/mL) in DMEM for 12 h, followed with the incubation of Lysotracker DND 99 (100 nM) or BODIPY (10 μM) in DMEM for 30 min. Then, the spices were observed on CLSM. The same treatments were carried for NIH 3T3 and ktr-3 cells.

Oleic acid treatment: HeLa cells were treated with oleic acid (10 μg/mL) in DMEM (10% FBS) for 6 h, followed with the incubation of TPA-BTTDO NPs (2.4 μg/mL) in DMEM for 12 h. Then, HeLa cells were furtherly treated with BODIPY (10 μM) in DMEM for 30 min. TPA-BTTDO NPs: λ_{ex} = 405 nm, λ_{em} = 450–725 nm. BODIPY: λ_{ex} = 488 nm, λ_{em} = 510–540 nm. Lysotracker DND 99: λ_{ex} = 543 nm, λ_{em} = 570–650 nm. Overlap coefficient and Pearson correlation coefficient were analyzed on Zeiss LSM 710.

4.6. Internalization speed of NPs by HeLa cells

HeLa cells were incubated with TPA-BTTDO NPs (2.4 μg/mL) in DEME for 2, 4, 12 and 24 h, respectively. After washed by PBS for three times, HeLa cells were incubated with Lysotracker (100 nM) in DMEM for 30 min, followed by characterization with CLSM.

4.7. Endocytosis inhibition assay

After washed by PBS for three times, HeLa cells were treated by Dynasore (100 μM) for 1 h, Chlorpromazine (5 μg/mL) for 30 min, cytochalasin D (10 μg/mL) for 30 min, nystatin (15 μM) for 1 h or Sucrose (150 mM) for 1 h, respectively. HeLa cells without any treatment was set as control. Then, the cells were incubated with TPA-BTTDO NPs (4 μM) in DMEM for 4 h under 37 °C. One group of cells wthout treatment was cultured under 4 °C. After washed by PBS for three times, HeLa cells were characterized under CLSM.

4.8. The tracing of LDs dynamic movements and consumption

HeLa cells were treated by oleic acid (10 μg/mL) in DMEM (10% FBS) for 6 h, followed with the incubation of TPA-BTTDO NPs in DMEM for 12 h. The movement was studied by CLSM every 30 s. Meanwhile, HeLa cells were imaged every 24 h with the lambda-scanning mode. At the fourth day, cells were costained with Lysotracker (100 nM) or Mitotracker (1 μM). Mitotracker: λ_{ex} = 543 nm, λ_{em} = 570–650 nm.

Acknowledgments

This work was financially supported by the National Natural Science Foundation of China (21788102 and 21673082), the Guangdong Natural Science Funds for Distinguished Young Scholar (2014A030306035), the Natural Science Foundation of Guangdong Province (2016A030312002), the Innovation and Technology Commission of Hong Kong (ITC-CNERC14SC01), Science & Technology Program of Guangzhou (201804020027 and 201804010218), the Fundamental Research Funds for the Central Universities (2017B0036) and the China Postdoctoral Science Foundation (2017M612647).

Appendix A. Supplementary data

Supplementary data to this article can be found online at https://doi.org/10.1016/j.biomaterials.2019.03.002.

References

[1] F. Wilfling, J.T. Haas, T.C. Walther, R.V.F. Jr, Lipid droplet biogenesis, Curr. Opin. Cell Biol. 29 (2014) 39–45.
[2] Y. Guo, T.C. Walther, M. Rao, N. Stuurman, G. Goshima, K. Terayama, J.S. Wong, R.D. Vale, P. Walter, R.V. Farese, Functional genomic screen reveals genes involved in lipid-droplet formation and utilization, Nature 453 (2008) 657–661.
[3] Y. Miyanari, K. Atsuzawa, N. Usuda, K. Watashi, T. Hishiki, M. Zayas, R. Bartenschlager, T. Wakita, M. Hijikata, K. Shimotohno, The lipid droplet is an important organelle for hepatitis C virus production, Nat. Cell Biol. 9 (2007) 1089–1097.
[4] P.T. Bozza, I. Bakker-Abreu, R.A. Navarro-Xavier, C. Bandeira-Melo, Lipid body function in eicosanoid synthesis: an update, Prostaglandins Leukot. Essent. Fatty Acids 85 (2011) 205–213.
[5] R.S. Ahima, Digging deeper into obesity, J. Clin. Investig. 121 (2011) 2076–2079.
[6] X. Li, J. Ye, L. Zhou, W. Gu, E.A. Fisher, P. Li, Opposing roles of cell death-inducing DFF45-like effector B and perilipin 2 in controlling hepatic VLDL lipidation, J. Lipid Res. 53 (2012) 1877–1889.
[7] R. Chowdhury, B. Jana, A. Saha, S. Ghosh, K. Bhattacharyya, Confocal microscopy of cytoplasmic lipid droplets in a live cancer cell: number, polarity, diffusion and solvation dynamics, Med. Chem. Comm. 5 (2014) 536–539.
[8] H. Abramczyk, J. Surmacki, M. Kopeć, A.K. Olejnik, K. Lubecka-Pietruszewska, K. Fabianowska-Majewska, The role of lipid droplets and adipocytes in cancer. Raman imaging of cell cultures: MCF10A, MCF7, and MDA-MB-231 compared to adipocytes in cancerous human breast tissue, Analyst 140 (2015) 2224–2235.
[9] R. Zimmermann, J.G. Strauss, G. Haemmerle, G. Schoiswohl, R. Birner-Gruenberger, M. Riederer, A. Lass, G. Neuberger, F. Eisenhaber, A. Hermetter, R. Zechner, Fat mobilization in adipose tissue is promoted by adipose triglyceride lipase, Science 306 (2004) 1383–1386.
[10] R. Singh, S. Kaushik, Y. Wang, Y. Xiang, I. Novak, M. Komatsu, K. Tanaka, A.M. Cuervo, M.J. Czaja, Autophagy regulates lipid metabolism, Nature 458 (2009) 1131–1135.
[11] H. Dong, M.J. Czaja, Regulation of lipid droplets by autophagy, Trends Endocrinol. Metabol. 22 (2011) 234–240.
[12] I. Dugail, Lysosome/lipid droplet interplay in metabolic diseases, Biochimie 96 (2014) 102–105.
[13] L. Xu, L.K. Zhou, P. Li, CIDE proteins and lipid metabolism, Arterioscler. Thromb. Vasc. Biol. 32 (2012) 1094.
[14] H.F. Hashemi, J.M. Goodman, The life cycle of lipid droplets, Curr. Opin. Cell Biol. 33 (2015) 119–124.
[15] C. Yao, P. Wang, X. Li, X. Hu, J. Hou, L. Wang, F. Zhang, Near-infrared-triggered azobenzene-liposome/upconversion nanoparticle hybrid vesicles for remotely controlled drug delivery to overcome cancer multidrug resistance, Adv. Mater. 28 (2016) 9341–9348.
[16] S. Li, Q. Li, Y. Kong, S. Wu, Q. Cui, M. Zhang, S.O. Zhang, Specific regulation of thermosensitive lipid droplet fusion by a nuclear hormone receptor pathway, Proc. Natl. Acad. Sci. U. S. A 114 (2017) 8841–8846.
[17] J. Murray, J. Sim, K. Oh, G. Sung, A. Lee, A. Shrinidhi, A. Thirunarayanan, D. Shetty, K. Kim, Enrichment of specifically labeled proteins by an immobilized host molecule, Angew. Chem. Int. Ed. 129 (2017) 2435–2438.
[18] J. Ni, H. Liu, J. Liu, M. Jiang, Z. Zhao, Y. Chen, R.T.K. Kwok, J.W.Y. Lam, Q. Peng, B.Z. Tang, The unusual aggregation-induced emission of coplanar organoboron isomers and their lipid droplet-specific applications, Mater. Chem. Front. 2 (2018) 1498–1507.
[19] Y. Zhang, Y. Wang, J. Wang, X.-J. Liang, Improved pharmaceutical research and development with AIE-based nanostructures, *Mater. Horiz.* 5 (2018) 799–812.

[20] J. Gong, Z. Sun, L. Wu, W. Xu, N. Schieber, D. Xu, G. Shui, H. Yang, R.G. Parton, P. Li, Fsp27 promotes lipid droplet growth by lipid exchange and transfer at lipid droplet contact sites, J. Cell Biol. 195 (2011) 953–963.
[21] S. Harchouni, B. Field, B. Menand, AC-202, a highly effective fluorophore for the visualization of lipid droplets in green algae and diatoms, Biotechnol. Biofuels 11 (2018) 120.
[22] T.K. Mukhopadhyay, A. Datta, Ordering and dynamics for the formation of two-dimensional molecular crystals on black phosphorene, J. Phys. Chem. C 121 (2017) 10210–10223.
[23] L. Guo, M. Tian, R. Feng, G. Zhang, R. Zhang, X. Li, Z. Liu, X. He, J.Z. Sun, X. Yu, Interface-targeting strategy enables two-photon fluorescent lipid droplet probes for high-fidelity imaging of turbid tissues and detecting fatty liver, ACS Appl. Mater. Interfaces 10 (2018) 10706–10717.
[24] A.A.R. Mota, P.H.P.R. Carvalho, B.C. Guido, H.C.B. de Oliveira, T.A. Soares, J.R. Corrêa, B.A.D. Neto, Bioimaging, cellular uptake and dynamics in living cells of a lipophilic fluorescent benzothiadiazole at low temperature (4 °C), Chem. Sci. 5 (2014) 3995–4003.
[25] Y. Lee, W. Cho, J. Sung, E. Kim, S.B. Park, Monochromophoric design strategy for tetrazine-based colorful bioorthogonal probes with a single fluorescent core skeleton, J. Am. Chem. Soc. 140 (2018) 974–983.
[26] Z. Liu, X. Li, Q. Ge, M. Ding, X. Huang, A lipid droplet-associated GFP reporter-based screen identifies new fat storage regulators in C. elegans, J. Genet. Genomics 41 (2014) 305–313.
[27] (a) H.J.R. Fernandes, Beyond the lysosome: cholesterol role on endoplasmic reticulum and lipid droplets in Parkinson's disease, Mov. Disord. 33 (2018) 342-342;
(b) Y. Ohsaki, Y. Shinohara, M. Suzuki, T. Fujimoto, A pitfall in using BODIPY dyes to label lipid droplets for fluorescence microscopy, Histochem. Cell Biol. 133 (2010) 477–480.
[28] (a) C. Zhang, L. Yang, Y. Ding, Y. Wang, L. Lan, Q. Ma, X. Chi, P. Wei, Y. Zhao, A. Steinbuchel, H. Zhang, P. Liu, Bacterial lipid droplets bind to DNA via an intermediary protein that enhances survival under stress, Nat. Commun. 8 (2017) 15979;
(b) X. Zhang, K. Wang, M. Liu, X. Zhang, L. Tao, Y. Chen, Y. Wei, Polymeric AIE-based nanoprobes for biomedical applications: recent advances and perspectives, Nanoscale 7 (2015) 11486–11508;
(c) Z. long, L. Mao, M. Liu, Q. Wan, X. Zhang, Y. Wei, Marrying multicomponent reactions and aggregation-induced emission (AIE): new directions for fluorescent nanoprobes, Polym. Chem. 8 (2017) 5644–5654.
[29] (a) Y. Wang, S. Li, P. Zhang, H. Bai, L. Feng, F. Lv, L. Liu, S. Wang, Photothermal-Responsive conjugated polymer nanoparticles for remote control of gene expression in living cells, Adv. Mater. 30 (2018) 1705418;
(b) A.M. Valm, S. Cohen, W.R. Legant, J. Melunis, U. Hershberg, E. Wait, A.R. Cohen, M.W. Davidson, E. Betzig, J. Lippincott-Schwartz, Applying systems-level spectral imaging and analysis to reveal the organelle interactome, Nature 546 (2017) 162–167;
(c) M. Schuldiner, M. Bohnert, A different kind of love – lipid droplet contact sites, BBA-Mol. Cell Biol. L. 1862 (2017) 1188–1196.
[30] (a) B. Chen, J. Zeng, Y. Xiong, H. Nie, W. Luo, Z. Zhao, B.Z. Tang, Synthesis, aggregation-induced emission and electroluminescence of new luminogens based on thieno[3,2-b]thiophene S,S-dioxide, Dyes Pigments 159 (2018) 275–282;
(b) M. Kastantin, B. Ananthanarayanan, P. Karmali, E. Ruoslahti, M. Tirrell, Effect of lipid chain melting transition on the stability of DSPE-PEG (2000) micelles, Langmuir 25 (2009) 7279–7286.
[31] (a) M. Jiang, X. Gu, J.W.Y. Lam, Y. Zhang, R.T.K. Kwok, K.S. Wong, B.Z. Tang, wo-photon AIE bio-probe with large Stokes shift for specific imaging of lipid droplets, Chem. Sci. 8 (2017) 5440–5446;
(b) Q. Chen, H. Wang, H. Liu, S. Wen, C. Peng, M. Shen, G. Zhang, X. Shi, NanoparticlesModified with RGD peptide for targeted computed tomography/magnetic resonance dual-modal imaging of tumors, Anal. Chem. 87 (2015) 3949–3956;
(c) Y. Cheng, J. Dai, C. Sun, R. Liu, T. Zhai, X. Lou, F. Xia, Intracellular H_2O_2-responsive AIEgen with peroxidase-mediated catalysis for inflammatory cell selective imaging and inhibition, Angew. Chem. Int. Ed. 57 (2018) 3123–3127.
[32] (a) M. Gao, H. Su, S. Li, Y. Lin, X. Ling, A. Qin, B.Z. Tang, An easily accessible aggregation-induced emission probe for lipid droplet-specific imaging and movement tracking, Chem. Commun. 53 (2017) 921–924;
(b) Y. Wang, R. Hu, W. Xi, F. Cai, S. Wang, Z. Zhu, R. Bai, J. Qian, Red emissive AIE nanodots with high two-photon absorption efficiency at 1040 nm for deep-tissue in vivo imaging, Biomed. Opt. Express 6 (2015) 3783–3794.
[33] (a) C.W.T. Leung, Z. Wang, E. Zhao, Y. Hong, S. Chen, R.T.K. Kwok, A.C.S. Leung, R. Wen, B. Li, J.W.Y. Lam, B.Z. Tang, A lysosome-targeting AIEgen for autophagy visualization, Adv. Healthc. Mater. 5 (2016) 427–431;
(b) R. Zhan, Y. Pan, P.N. Manghnani, B. Liu, AIE polymers: synthesis, properties, and biological applications, Macromol. Biosci. 17 (2017) 1600433.
[34] M. Gao, H. Su, Y. Lin, X. Ling, S. Li, A. Qin, B.Z. Tang, Photoactivatable Aggregation-induced emission probes for lipid droplets-specific live cell imaging, Chem. Sci. 8 (2017) 1763–1768.
[35] N. Alifu, X. Dong, D. Li, X. Sun, A. Zebibula, D. Zhang, G. Zhang, J. Qian, Aggregation-induced emission nanoparticles as photosensitizer for two-photon photodynamic therapy, Mater. Chem. Front. 1 (2017) 1746–1753.
[36] E. Wang, E. Zhao, Y. Hong, J.W.Y. Lam, B.Z. Tang, A highly selective AIE fluorogen for lipid droplet imaging in live cells and green algae, J. Mater. Chem. B 2 (2014) 2013–2019.